March 2004

The creation of organic and biological nanostructures at surfaces using scanning probe nanolithography

B. L. Weeks
Lawrence Livermore National Laboratory, Livermore, CA

Chin Li Cheung
University of Nebraska at Lincoln, ccheung2@unl.edu

J. J. De Yoreo
Lawrence Livermore National Laboratory, Livermore, CA

Published in *Nanoscale Structure and Assembly at Solid-Fluid Interfaces: Volume II, Assembly in Hybrid and Biological Systems*, edited by Xiang Yan Liu and James J. De Yoreo. Boston/Dordrecht/ New York/London: Kluwer Academic Publishers, 2004.

8

The creation of organic and biological nanostructures at surfaces using scanning probe nanolithography

B.L. Weeks, C.L. Cheung, J.J. De Yoreo*
Biosecurity and Nanosciences Laboratory, Chemistry and Materials Science Directorate, Lawrence Livermore National Laboratory, Livermore, CA 94551, USA

8.1. INTRODUCTION

As the size of microelectronic devices continues to shrink and the desire to build in hierarchical structures of organic and biological materials grows, control of the chemistry and structure of materials at the molecular level will become increasingly important. Conventional lithographic techniques to pattern polymeric thin films are beginning to reach their resolution limit and several alternative "bottom-up" strategies have emerged that use the scanning probe microscope to manipulate matter at the atomic or molecular scale. Of these new scanning probe nanolithography (SPN) techniques, dip-pen nanolithography (DPN) [1] and scanning probe nanografting (SNG) [2] are particularly promising.

The DPN methodology utilizes the tip of an atomic force microscope (AFM) as a "nanopen" to transport an "ink" containing organic molecules onto a solid support as illustrated in Figure 8.1. Using the same tip to "write" and subsequently "read" patterns, it is possible to create nanoscale patterns of alkyl thiols with remarkable resolution (~10 nm) and simultaneously control the chemical functionality of the written areas. Examples of patterns created using a variety of inks are shown in Figure 8.2.

The SNG methodology also relies on an AFM tip to pattern the surface, but in this case the substrate is first uniformly functionalized with a layer of one kind of ink, and the tip is used to remove portions of that layer, which are then filled in by a second ink to create patterns with multiple functionality. Removal and re-deposition are done either in a single step by operating in the presence of a solution containing the second ink, which fills in

*Corresponding author. E-mail address: deyoreo1@llnl.gov

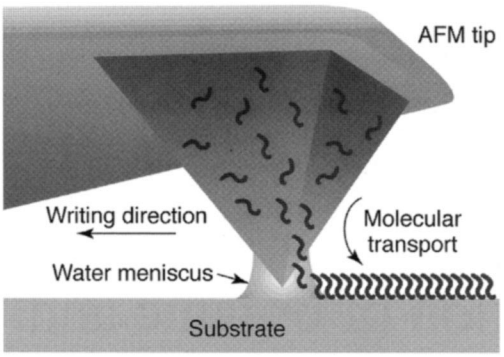

FIGURE 8.1. Schematic of the dip pen nanolithography process. Ink molecules coated onto an AFM tip are deposited as the tip moves across a substrate.

behind the tip, or they are performed in a two-step process in which removal is done in air and followed by subsequent exposure of the substrate to a solution of the second ink. Both methods also give feature sizes down to ~10 nm. The two-step nanografting process is illustrated in Figure 8.3, and an example of a two-ink SNG pattern is given in Figure 8.4.

This technology provides a particularly attractive tool for nanostructural engineering because it immediately lends itself to construction of an inorganic–organic interface that is controlled at the atomic scale by the nature of the intermolecular interactions between the ink molecules, as well as at the nanoscale by the inherent size of the tip–surface contact. Moreover, because alkyl chains can readily be synthesized with a variety of functionalities in the head group, SPN provides a route towards constructing hierarchical nanostructures comprised of inorganic substrates, organic linkers, and biological molecules such as proteins, DNA, and even whole organisms. Indeed, as this chapter will show, patterning of all three at length scales of 100 nm or less have already been achieved.

8.2. DEVELOPMENT OF SCANNING PROBE NANOLITHOGRAPHY

The break-through that has allowed for the formation of these soft structures is scanning probe microscopy. The grandfather of all scanning probe techniques is the scanning tunneling microscope (STM) [3]. Scanning tunneling microscopy is an analytical technique based on the detection of a quantum mechanical tunneling current between a tip and a sample. When the tip is brought within about 10 Å of the sample, electrons begin to "tunnel" across the gap. Because the resulting tunneling current varies strongly with tip-to-sample spacing, the variations in this current can be used to create an image of the surface. Changes in surface features of about 1 Å cause the tunneling current to change by almost an order of magnitude. It is this relationship that gives STM the ability to obtain true atomic resolution on conducting and semi-conducting surfaces. Unfortunately, there are some limitations with STM. The most significant is that both the surfaces of the tip and sample must be conducting, limiting the types of materials that can be studied. This limitation helped to drive the invention of the first atomic force microscope in 1986.

Like STM, AFM also uses a very sharp tip to probe the surface. However, in AFM there is no requirement to measure a current flowing between the tip and sample, which allows

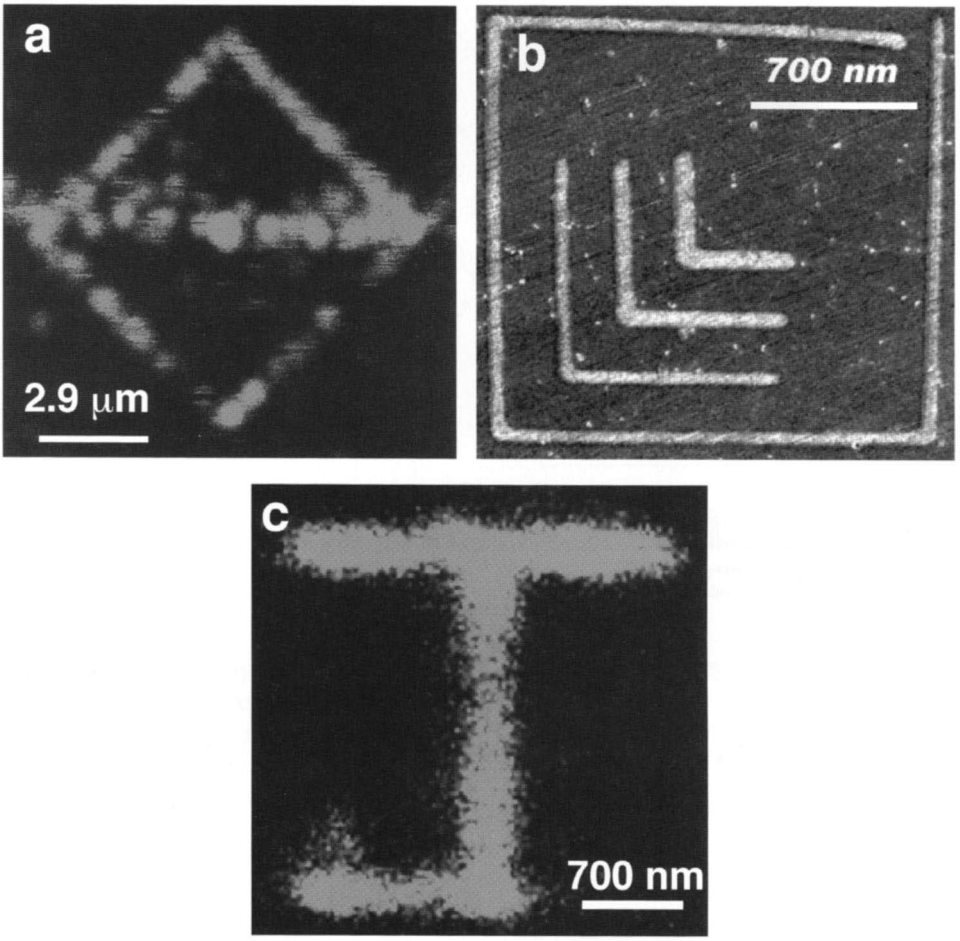

FIGURE 8.2. Examples of structures created with dip pen nanolithography: (a) scanning confocal image of Rhodamine 6G patterned with DPN on a glass substrate; (b) friction force image of 16-mercaptohexadecanoic acid on a gold substrate; (c) scanning confocal microscopy image of a HCG antibody pattern fabricated on glass. Probe translation speed was 0.2 $\mu m\,s^{-1}$. Each line in the pattern was overwritten ten times to maximize the protein surface density. Note that in the confocal images, the apparent line-width is determined by the resolution of the confocal system which is about 500 nm. In the case of Rhodamine 6G, fluorescent signals from single molecules are observed.

one to image both conducting and non-conducting samples. The first AFM was made by meticulously gluing a tiny sliver of diamond onto one end of a strip of foil to form a micro cantilever, which was then used to examine insulating surfaces [4]. The results were staggering, demonstrating lateral resolution at insulating surfaces on the order of 300 Å. However, without a breakthrough in tip manufacturing, the AFM probably would have remained a curiosity in many research groups. It was Albrecht *et al.* who fabricated the first silicon microcantilever and measured the atomic structure of boron nitride [5]. Today, most commercial cantilevers are mass-produced with optical lithographic techniques and are constructed from Si or Si_3N_4. Figure 8.5 shows an SEM micrograph of a silicon cantilever.

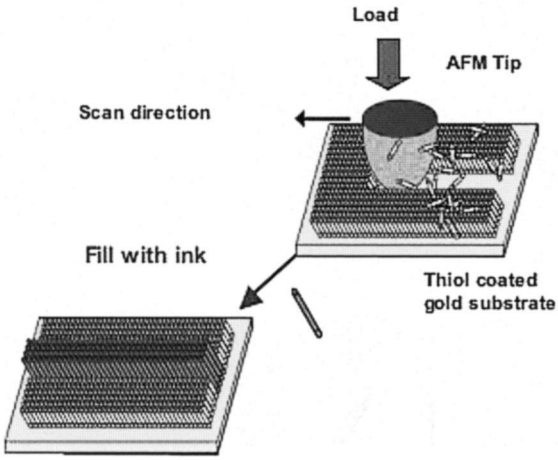

FIGURE 8.3. Schematic of the two-step nanografting process. A substrate is initially coated with a self-assembly monolayer (SAM), which is then locally removed by the AFM tip. Subsequent exposure to a solution containing a second ink results in a two-phase SAM.

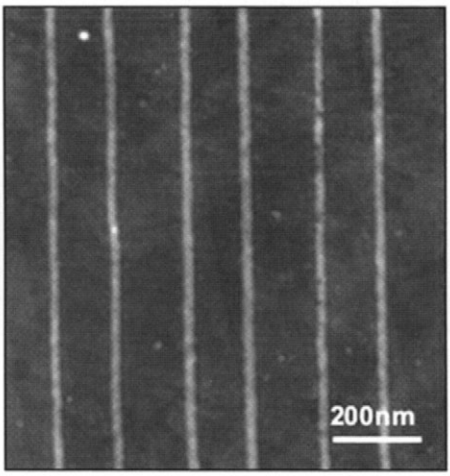

FIGURE 8.4. AFM image of alkyl thiols patterned on a gold substrate. Darker regions are coated with a self-assembly monolayer of polyethylene glycol terminated alkyl thiol. The lines are regions containing longer chain, amino terminated alkyl thiols.

The force between an AFM tip and sample surface during imaging is very small, usually less than 10^{-9} N. But the detection system does not measure this force directly. Instead it senses the deflection of the microcantilever, which follows Hook's law. The detecting systems for monitoring the deflection fall into several categories. The first device introduced by Binnig was a tunneling tip placed above the surface of a cantilever that had been metallized. As with the STM, a change in spacing of 1 Å between tip and cantilever changed the tunneling current by an order of magnitude. Thus, it was straightforward to measure deflections smaller than 0.01 Å. Subsequent systems were based on optical techniques. The interferometer is the most sensitive of the optical methods, but it is somewhat more

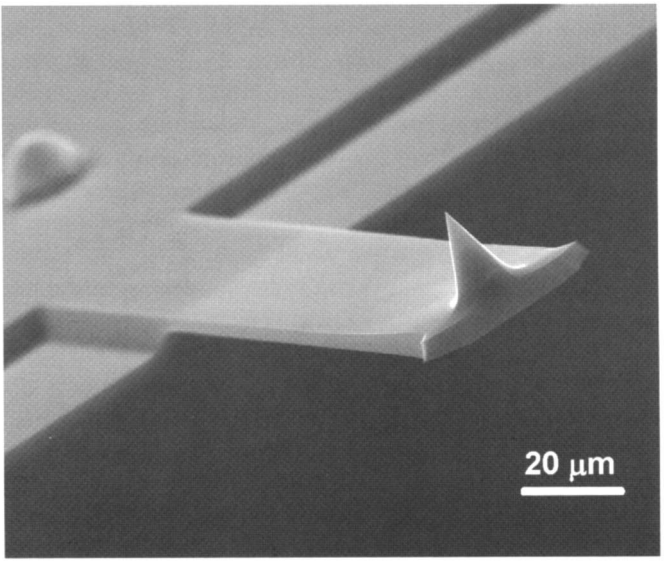

FIGURE 8.5. A scanning electron microscopy image of a silicon cantilever.

complicated than the optical lever, which was introduced by Meyer and Amer [6]. In the latter, visible light from a low power laser diode is focused on the apex of a cantilever. The light is then reflected from the mirrored surface on the backside of the cantilever onto a position-sensitive photodetector. The distance traveled by the laser beam is proportional to the cantilever deflection and magnified by the cantilever-photodetector distance as the arm of a lever. By far the most common method of detection used by commercial AFMs is the optical lever with a four-quadrant photo detector [7] as shown in Figure 8.6. By using a four-quadrant photo detector both cantilever deflection (which reflects the sample topography) and cantilever twisting (which occurs in response to friction forces between tip and surface) can be measured simultaneously.

Early in the development of the STM, scientists began to use it as a tool for creating topographical structures on various surfaces. Methods included localized chemical vapor deposition [8], electrodeposition [9], mechanical contact of the tip with the surface [10], and deformation of the surface by electrical pulses in both vacuum and elevated pressures [11,12]. The majority of STM lithography experiments focused on producing the smallest possible structures. Perhaps the most delicate examples of nanofabrication to date are the atomic structures formed by using the STM to deposit individual xenon atoms on nickel [13].

AFM-based lithography affords somewhat less precision and resolution than that obtained with STM lithographic techniques, but opens the door to manipulation of nonconducting surfaces. The AFM can also be used to modify surfaces locally via electrodeposition or catalytic chemical reactions [9,10]. However, one of the main advantages of AFM-based lithography results from the contact between tip and surface, which enables one to produce physical deformation of surfaces at a local scale. In typical AFM contact imaging the forces exerted on the surface are on the order of 0.05 nN. But increasing the local pressure will eventually lead to a surface deformation. In the case of an alkyl thiol

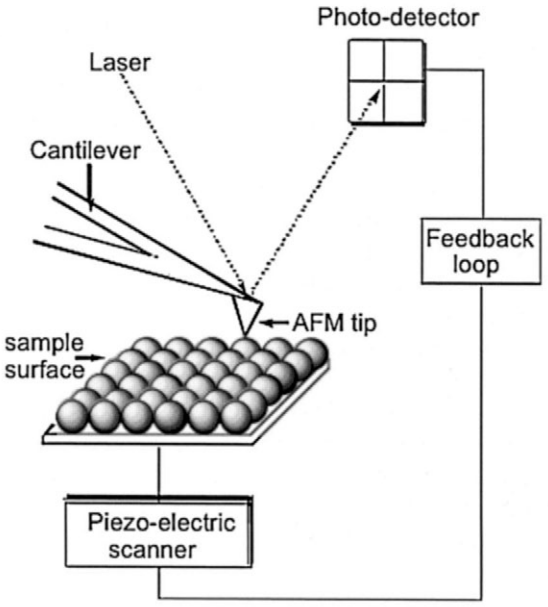

FIGURE 8.6. Diagram of an atomic force microscope with optical lever detection and a four-quadrant photodetector.

coated gold surfaces, the tip can be used like a "snowplow" to locally remove a monolayer of the self-assembled monolayer (SAM), which is the basis of SNG. With increasing pressure, the tip first causes deformation, then disrupts the alkyl thiol packing, and eventually displaces the alkyl thiol molecules at the adsorption site because the Au–S bond is the weakest one at the interface. (The binding energies for S–Au, C–C, C–H, and C–S are 40, 145, 81, and 171 kcal/mol, respectively. In addition, the lateral movement of thiols on gold requires less activation energy than does desorption.) Increasing the load still further causes the underlying gold substrate to deform.

8.3. DIP PEN NANOLITHOGRAPHY

The other advantage of the tip surface contact that the AFM provides, is the ability to directly transfer molecules from tip to surface, which is the basis of DPN. The discovery of DPN came from studies of the dynamics of the capillary effect and water transport from an AFM tip in air [14]. From that work, Piner and Mirkin were able to demonstrate that by bringing the tip of an AFM in contact with a surface would cause depletion or an increase in the amount of water on the surface dependent on the surface energy, contact time, and initial humidity. The structures formed were only observable for approximately a day depending on humidity, temperature, size of feature, etc. Using the meniscus that naturally forms in air between the tip and sample as a transport medium provided a way of controlling molecular deposition from a coated AFM tip onto the substrate. By carefully choosing molecules that were designed to react with the surface to be patterned, they created a chemical driving force favoring the transfer of such molecules to the substrate. Chemisorption of the ink

molecules onto the substrate led to stable nanostructures, which would not degrade over time as was the case in the experiments using water condensation.

The first demonstration of DPN showed that alkyl thiols could be patterned onto gold surfaces and that regulating humidity and temperature led to control over the feature size. Hydrophilic and hydrophobic molecules—including biomolecules such as DNA and proteins—have now been patterned via the DPN process [15,16]. Moreover, through the development of controlled-environmental chambers, which allow one to replace the water meniscus with other solvents, it seems likely that it will be possible to extend DPN to a wide range of molecular species and substrates.

One feature that sets DPN apart from other high resolution nanolithographic techniques is its registration capabilities. Since one uses the same AFM cantilever to write the pattern and subsequently read the image, one can generate multiple nanostructures, made of the same or different inks, and align them with respect to one another with nanometer-scale precision. This capability makes DPN an excellent tool for generating multifunctional nanostructures and for making chips with integrated soft lithographic molecules comprised of different chemical components. For this reason, DPN could have a major impact in molecular electronics, bioinformatics, catalysis, and sensor design. With commercially available cantilevers, DPN currently offers 15 nm line-width and 5 nm spatial resolution and, therefore, rivals other techniques such as e-beam lithography for patterning solid substrates while having the advantage of not requiring a vacuum to operate.

One of the largest drawbacks of DPN is that it is an inherently a serial process. Most researchers use a single cantilever, which limits the size of the lithographic pattern being formed to that of the scan range of the AFM. Recently, DPN has been partially transformed from a serial to parallel process through the use of eight cantilevers, and arrays of 10,000 cantilevers have now been produced for the next generation of DPN machines. Because the feature dimensions in a DPN experiment are almost independent of the tip/sample contact force over a range of two orders of magnitude, an array of tips can be used in a parallel writing fashion by engaging all of the tips in the array with the substrate to be patterned. Through careful design, it seems likely that each of these tips can be engaged individually to allow the multiple pen system to be used in serial fashion like a nanoplotter, where each of the tips has a different ink.

Although DPN is particularly well suited for patterning flat solid substrates with soft matter, it has been combined with wet chemical etching procedures to fabricate silicon structures, thus far on a length scale greater than 40 nm. Recently, silicon nanostructures were generated via a multi-step process that utilizes DPN to generate soft resist structures comprised of octadecane thiol (ODT) on gold /titanium/silicon layered structures [17]. The areas that were coated with the ODT layers were resistant to the etchant (ferrocyanide-based solution) while the unmodified gold could be selectively etched, to leave behind an alkyl thiol-capped gold surface. The exposed titanium-coated silicon were subsequently etched with KOH. Removing the Au and Ti layers with *aqua regia* yielded a 3D modified bare silicon surface. This approach, in principle, could be extended to other metal-coated substrates or doped silicon to produces conducting circuits with features much smaller than currently available through commercial photolithography.

DPN can also be used for combinatorial chemistry experiments at the nanoscale [18]. Essentially, the instrument can be programmed to generate a series of monolayer patterns that vary with respect to composition, feature size, and feature spacing. These patterns

subsequently can be used to study a wide range of chemical or physical processes. These include crystallization, catalysis, chemical and biochemical recognition, etching behavior, surface molecular transport, and many others. One can determine the type of pattern appropriate for a given application and then, because of the dimensions associated with these patterns, the same scanning probe instrument used to generate them can be used to screen thousands on a relatively fast time scale. This combinatorial-nanotechnology approach has the potential to change the way we explore many nanoscale phenomena and, therefore, have a major impact on the development of new technologies based on materials with sub-100 nm dimensions.

Although DPN is still in its infancy, its development already has led to the accomplishment of several important milestones in nanotechnology and in scanning probe nanolithographies in particular. First, it is now a user-friendly form of lithography accessible to any group with a conventional AFM. This alone should accelerate its use throughout the scientific community at large and especially within the chemical and biochemical communities. Second, its direct-write nature sets it apart from other scanning probe lithography alternatives and provides some unique capabilities with respect to nanostructure registration and the chemical complexity one can incorporate into soft nanostructures. Third, it offers comparable resolution to optical lithography, but it is substantially more general with respect to the types of structures (hard and soft) one can pattern. With the incorporation of multiple probes, it offers parallel writing capabilities with minimal increase in the complexity of the patterning instrumentation. The challenge facing future development of DPN is its advancement from an academic curiosity to a highly-automated, massively-parallel workhorse for industry.

8.4. SCANNING PROBE NANOGRAFTING

Due to the similarity of the two methods, much of the discussion about DPN also applies to SNG, which was also developed at about the same time as DPN. The resolution limit is quite similar. However, Liu *et al.* used SNG, to create nano-islands with dimensions of 3 nm by 5 nm, making these the smallest AFM-based SPN structures yet reported [2]. Moreover, they have shown that SNG features can be erased and recreated simply by performing a second SNG experiment on the feature to be erased while using the original ink to fill in behind the tip. Using both one and two-step nanografting methods, patterns of alkane thiols, proteins, and DNA have all been formed [19,20].

Because SNG is performed by first covering the entire substrate with an initial SAM, DPN affords somewhat greater flexibility than nanografting. However, the fidelity and reproducibility of DPN is inherently worse than in SNG. This is because both the coverage of ink on the tip as well as the ink transfer rate are sensitive to a myriad of factors including ink composition, coating methodology, humidity, temperature, and deposition time or writing speed. (The reasons for these dependencies will be discussed below.) In SNG, while ink deformation and removal is done locally by the tip (and can be well controlled by maintaining constant force), ink deposition is actually a bulk chemical process that ensures high uniformity. For this reason, SNG offers some advantages when developing inks or methods for using those inks as templates to create hierarchical structures. But inks that are successful with one method are generally transferable to the other.

8.5. PHYSICAL MODELS OF INK TRANSFER DURING DPN

A variety of factors could determine the feature size achieved during DPN. These factors include dwell time, writing speed, temperature, tip coverage, interfacial tension, and humidity. Recently, a number of researchers have used measurements of feature size in an attempt to both assess some of these factors and create a physical model of ink transfer from tip to substrate. Nonetheless, a complete picture of the physical processes and materials parameters that control transfer and deposition has yet to emerge. For example, there is a controversy over whether a water meniscus is needed for this transfer. DPN patterns of ODT have been fabricated in 0% relative humidity and show little or no dependence of feature size on humidity. In contrast, measurements of the dependence of feature size on humidity for 16-mercaptohexadecanoic acid (MHA) exhibit significant humidity effects. Indeed, many capillarity-related phenomena originate from the well-documented formation of water films on surfaces [21]. Thin water films have been studied by a variety of techniques including ellipsometry [22], NMR [23], adsorption isotherms [24], and atomic force microscopy [25]. These investigations have shown that the films are often just a few monolayers in thickness. When a water meniscus forms between an AFM tip and a surface, it has a profound effect on tip–sample interactions, both degrading image quality and interfering with force measurements [26]. Consequently, the meniscus formed between the tip and surface has often been assumed to be a crucial feature DPN [27,28]. However, even in the case of MHA, where the importance of the meniscus is now widely accepted, there is still debate over the ink transfer mechanisms.

Some researchers have modeled the dependence of feature size on dwell time using a diffusion-controlled mechanism through the meniscus [29,30]. But these models have ignored the dynamics of ink dissolution into the meniscus, a process which must be considered for soluble inks. Weeks *et al.* recently presented a model for MHA transfer that takes into account the ink dissolution kinetics [31]. Arrays of dots were fabricated by bringing an inked cantilever into contact with a freshly prepared gold surface. To minimize the transfer of MHA from the tip to the substrate, the sample was rastered at speeds greater than 4 Hz. To make a dot, the rastering was stopped and the tip was allowed to dwell at a specific location for a given time. The tip was then moved quickly to the next position and the process was repeated. In order to image the resulting pattern, the sample was rastered while recording the friction (lateral force) signal from the AFM. Figure 8.7 shows a typical friction image for an array of MHA dots deposited on gold. Experiments were repeated by varying the humidity from 0–55%. At a relative humidity at or below 15%, reproducible features were not observed for the shortest contact times (0.5 seconds and below) while for longer contact times we were able to produce features systematically at all contact times. Weeks *et al.* proposed that at that humidity the meniscus does not form between the tip and the sample, thus the ink transport to the surface is inhibited. However, subsequent experiments (by us) have shown that the meniscus takes time to form and that a meniscus can form even at low humidity. (Another possible explanation for the earlier result is that the gold used in these experiments was sputtered making grains that are larger than the smallest patterned features, making the features indistinguishable from the grains.)

Figure 8.8a shows the dependence of the dot area on dwell time for times between 0.5 s and 60 s and humidity ranging from 20% to 54%. Figure 8.8b shows the dependence of dot size on humidity for three different dwell times. Three features are evident. First, the

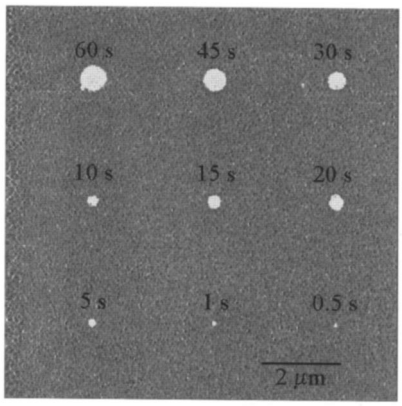

FIGURE 8.7. Friction-force image of MHA dots on gold fabricated with the indicated dwell times.

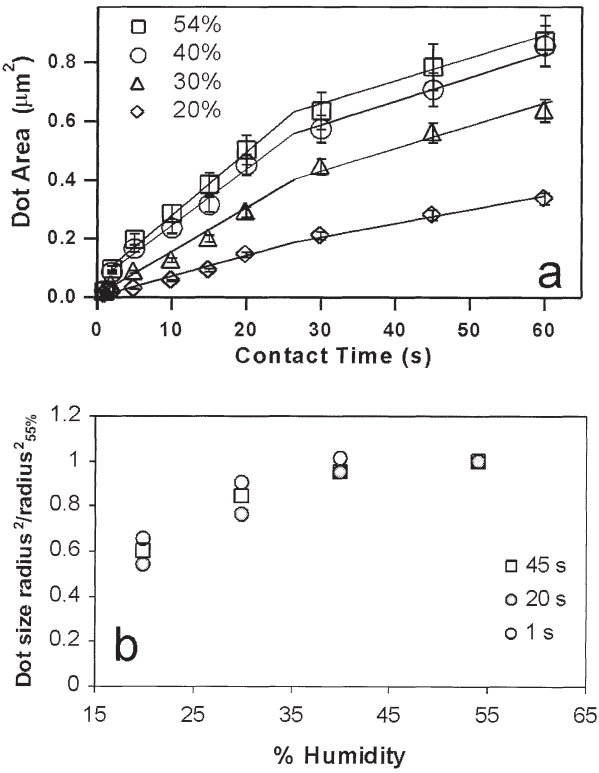

FIGURE 8.8. (a) Dependence of radius squared on dwell time as a function of relative humidity (H); (b) dependence of dot radius squared on humidity for three different dwell times normalized by the maximum radius squared at $H = 55\%$.

dependence of the square of the dot radius on dwell time is well fitted by two linear regions separated by a sharp transition zone which occurs over the same range of dwell times for all humidities. Second, from humidity of 20% to 45%, the spot size increases; while above

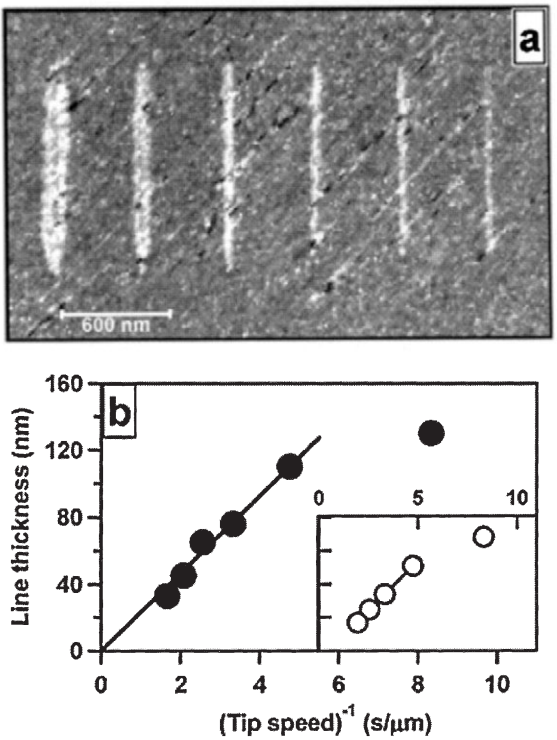

FIGURE 8.9. (a) Friction-force image of MHA lines on gold fabricated at tip speeds between 0.1 and 1 μm s^{-1}; (b) dependence of line width on inverse tip speed for both MHA and MEH-PPV (inset).

45% there is little change in the diameter of the spot. Third, the dependence of feature size on humidity is the same for all dwell times. At the highest humidity, the precision of the measurements decreased and the edges of the dots became less well defined. These results are consistent with lateral force microscopy and force spectroscopy studies [32,33].

In addition to dot fabrication, DPN can be used to write lines. In contrast to the case of dot generation where the tip is held stationary for the deposition time, during the fabrication of lines the tip continuously moves along the sample. In order to make a comparison between the controls on dot size and line width, lines were fabricated at tip speed, v, ranging from about 0.1 to 1 μm/s. The dependence of line width, W, on inverse speed, $1/v$, is presented in Figure 8.9. The data show a linear increase down to a speed of about 0.2 μm/s where the dependence weakens significantly. Data on line widths for the lines of poly[2-methoxy-5-(2′-ethyl-hexyloxy)-*p*-phenylene-vinylene] (MEH-PPV), a luminescent polymer, drawn on a SiO_2 surface are also given in the inset to show that this behavior is not peculiar to MHA.

To understand these experimental results Weeks *et al.* proposed the following model for ink transfer to the surface (Figure 8.10). The tip moves at constant speed, v,—which is zero for fabrication of dots—through a water film of thickness, δ, on the surface. Due to a non-zero contact angle at the tip, the height, h, of the meniscus at the tip, is different from δ. Thiol molecules dissolve from the tip into the meniscus, diffuse through the meniscus and

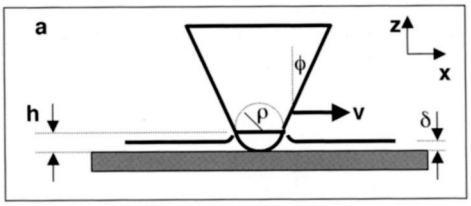

FIGURE 8.10. Schematic of the physical model for molecular transfer from AFM tip to substrate through meniscus of height h.

attach to the surface making a continuous self-assembled monolayer. After a time, τ, the tip is removed from the water film. At this time, thiol molecules are both attached to the surface and dissolved in the meniscus. Through diffusion, the dissolved thiols will eventually reach the edge of the SAM and attach to the substrate, contributing to the final feature size. Regardless of the tip-meniscus geometry, the magnitude of the diffusion constant, or the dissolution rate, the total number of molecules, N, transferred to the surface will be given by the integral of the transfer rate $\mathrm{d}N/\mathrm{d}t$ over the total tip–surface contact time τ.

For dot fabrication, two terms contribute to $\mathrm{d}N/\mathrm{d}t$: first, molecules dissolve from the tip through thermal activated detachment at a rate:

$$\left(\frac{\mathrm{d}N}{\mathrm{d}t}\right)_{+} = \frac{A}{\pi a^2}\beta_{+} = \frac{A}{\pi a^2}\nu e^{-E_{\mathrm{D}}/kT}, \tag{1}$$

where A is the contact area between the tip and the meniscus, πa^2 is the average area per thiol ink molecule, E_{D} is the activation energy for ink detachment, k is Boltzmann's constant, T is the temperature, and ν is an attempt frequency. In this case, the ink molecules are not detaching from the surface of a silicon nitride tip, rather they are detaching from the surface of a bulk alkane thiol solid that has precipitated onto the tip during the inking process. Second, molecules return to the tip simply due to impingement and attachment at a rate given by:

$$\left(\frac{\mathrm{d}N}{\mathrm{d}t}\right)_{-} = A\beta_{-}C_0 \approx A\left(\frac{kT}{2\pi m}\right)^{1/2} e^{-E_{\mathrm{A}}/kT}C_0, \tag{2}$$

where m is the mass of a thiol, E_{A} is the activation energy for attachment, and C_0 is the concentration of thiols in solution adjacent to the tip. The right hand side of eq. (2) assumes a gas kinetic expression for the impinging flux. A more complicated description would modify the factors in β_{-}, but will not change the dependence on C_0. (Note that in the absence of diffusion, C_0 will simply increase until it reaches the equilibrium solubility, C_{e}, at which time, $(\mathrm{d}N/\mathrm{d}t)_{+} = (\mathrm{d}N/\mathrm{d}t)_{-}$.)

The dot radius is related to N through $\pi R^2 = N\pi a^2$. Combining this relationship with eqs (1) and (2) and integrating gives:

$$R^2 = A\left(\beta_{+}\tau - \pi a^2\beta_{-}\int_0^{\tau} C_0(t)\mathrm{d}t\right). \tag{3}$$

Similar arguments lead to an expression for the dependence of line-width on tip speed. Assuming the tip moves over a distance l at a speed v, we write:

$$N = \int_0^l \left(\frac{\mathrm{d}N}{\mathrm{d}t}\right)\left(\frac{\mathrm{d}t}{\mathrm{d}x}\right)\mathrm{d}x = \frac{1}{v}\int_0^l \left(\frac{\mathrm{d}N}{\mathrm{d}t}\right)\mathrm{d}x. \tag{4}$$

The expressions for $(\mathrm{d}N/\mathrm{d}t)_+$ and $(\mathrm{d}N/\mathrm{d}t)_-$ remain the same as for dots, except that C_0 is now expressed as a function of v instead of t. Recognizing that $C_0(v)$ and β_- are both independent of x and that the line width $W = N\pi a^2/l$, eq. (4) becomes:

$$W = \left(\frac{A}{v}\right)\left(\beta_+ - \pi a^2 \beta_- C_0(v)\right). \tag{5}$$

For both dots and lines, the exact form of C_0 depends on a number of factors including the tip–meniscus geometry, surface attachment probability and the diffusivity, but because C_0 is small at short contact times or high tip speeds, two regimes emerge. For small τ (high v), $C_0 \approx 0$ and the dot size [(line-width)] is given by the first term in eq. (3) [(5)]. That is $R^2 \sim A\tau$ and $W \sim A/v$. This is the regime in which surface kinetics dominates the transfer process. For long contact times/slow tip speeds, C_0 reaches a limiting value C_0 that is less than C_e. Once again, $R^2 \sim A\tau$ and $W \sim A/v$, but the slopes of these linear relationships are reduced. In this regime the transfer process is controlled by diffusion. The predicted dependencies are similar to those observed for both dot and line fabrication (Figures 8.8 and 8.9).

The effect of humidity comes into this model through the impact of meniscus height, h, on contact area, A. The tip can be approximated by a cone terminated by a hemisphere of radius ρ. If $h \gg \rho$, A is approximately equal to that of a conical tip with half-cone angle ϕ, and height h, which is $\pi h^2 \sin\phi$. In contrast, for $h < \rho$, $A = 4\rho^2 \cos^{-1}(1 - h/\rho)$. For $h \ll \rho$, this has an $h^{0.5}$ dependence, while for $h \approx \rho$, it is linear in h. Consequently, as the humidity is increased from 15% to 50%, we expect the dot size to increase with a dependence that ranges from $h^{0.5}$ to h^2. Furthermore, because A is a multiplicative factor for both terms in eqs (3) and (5), in agreement with the measurements, the transition from dissolution-dominated to diffusion-dominated deposition should be independent of the humidity and the functional form of the dependence of dot radius on humidity should be the same for all dwell times (Figure 8.8).

An investigation of water film thickness performed on gold surfaces using scanning tunneling microscopy concluded that the film consisted of 30–50 nm islands that increased in thickness from about 2 nm at $H = 20\%$ to 10 nm at $H = 45\%$ [34]. Coincidentally, the increases in film thickness from that study, which are about a factor of four between H of 20% and 30% and about 1.4 between H of 30% and 40%, match the measured increases in dot size with humidity assuming an $h^{0.5}$ dependence in the low range, and an h^2 dependence in the high range.

One can quantitatively test the sensibility of this model to some degree by examining the low τ/ high v dependence of dot size and line width. In this regime, the slopes of R^2 vs. τ and W vs. $1/v$ are both given by $A\beta_+$. An upper limit for the attempt frequency, ν, is given by kT/h_p, where h_p is Planck's constant. This value is appropriate for simple atomic

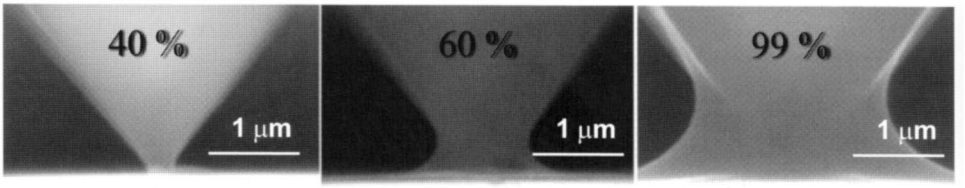

FIGURE 8.11. Environmental scanning electron microscopy (ESEM) images of an AFM tip in contact with a gold substrate. The relative humidity is noted in each image. The same tip was used for all images. The meniscus formed at 60% is approximately 400 nm in height while at 100% is nearly 2 μm. We cannot verify whether a meniscus forms at the low humidity range due to the resolution limit of the ESEM (approximately 75 nm under these conditions).

solids. In the case of chain-like molecules such as alkyl thiols, the attempt frequency is smaller. Although no detailed calculations of the appropriate frequency factor for these systems exist, models of idealized chain-like molecules lead to an estimate for ν, which is one to two orders of magnitude smaller. Taking the data for 20% to 54% relative humidity, using a range for n of 10^{10} to 6×10^{12} s^{-1}, and assuming the film thickness of 2 to 10 nm from Freund *et al.* [34] gives $E_D = 45$ to 60 kJ/mole for both the dots and the lines. This number should be greater than or equal to the heat of solution for MHA in water. Literature values for the heat of solution of a number of alkanes range from 25 to 40 kJ/mole [35,36].

As mentioned above, a number of researchers have found that a meniscus is not needed for creating features by DPN. Patterning of a number of molecules including MHA have been performed at relative humidity around 0%. In addition, experiments performed with octadecane thiol have shown little or no change on the patterning characteristics over a large range of relative humidity (~0 to 100%). One of the arguments against a role for the meniscus is that the Kelvin equation, which gives the size of the meniscus formed due to capillary condensation, predicts that the height of the meniscus should only be on the order of a few nanometers making it insufficient to account for the large feature sizes observed experimentally. However, environmental scanning electron microscopy images of a cantilever in contact with a surface show conclusively that the meniscus formed even at moderate humidity (40%) can be hundreds of nanometers to even many microns in height (Figure 8.11). Nonetheless, patterning at 0% can not be explained by transport through a meniscus (note that many molecules cannot be patterned at 0% including: DNA, dendrimers, and metal salts).

The obvious mechanism to explain patterning without a meniscus is that the molecules travel from the tip to the surface via surface diffusion as proposed by Sheehan *et al.* [37] and Schwartz [38] (see Figure 8.12a). In the case of ODT, it has been observed that there is no dependence of patterning rate on relative humidity. Moreover, the diffusion-based models appear to fit the data quite well. These data even predict a reasonable surface diffusion constant. In fact, Schwartz has proposed that humidity can actually impede the patterning rate of ODT. This "surface protection" effect provides a measurement of the special extent of the capillary meniscus as a function of relative humidity. In that work, Schwartz concluded that because ODT is not soluble in water, the lowest energy state would be for the ODT molecules to be at the air/water interface of the water meniscus. This effect has been proposed as the reason why a double line is produced by ODT under high humidity as seen in Figure 8.12b. By changing the vapor composition to ethanol, the molecules appear to

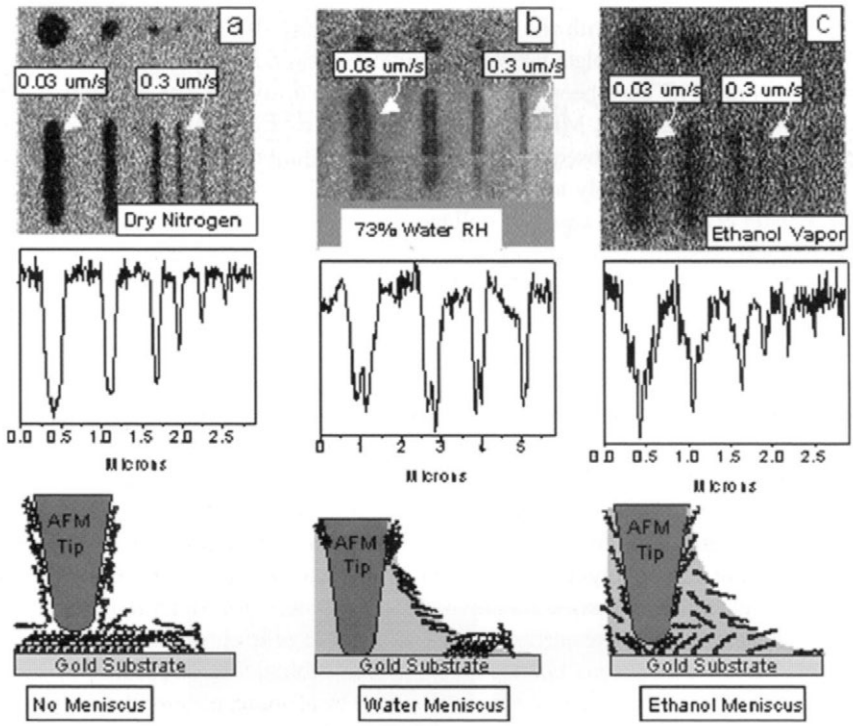

FIGURE 8.12. Effect of vapors on line profile. (a) Lines of ODT were DPN-generated and LFM imaged in a dry nitrogen environment; (b) lines of ODT were DPN-generated and LFM imaged in an environment high in water vapor; (c) lines of ODT were DPN-generated and LFM imaged in an environment of ethanol vapors. All experiments were done at room temperature. Below each LFM profile is a representation of the corresponding ODT molecular distribution that is consistent with both of the corresponding LFM profile as well as the bulk behavior of ODT.

readily diffuse through the meniscus as illustrated in Figure 8.12c. A very elegant model was presented by Schwartz in which the diffusion rate can be calculated by treating the patterning rate as a concentration gradient throughout the features being patterned.

8.6. USING SPN TEMPLATES TO CREATE HIERARCHICAL STRUCTURES

Methods for fabricating nanometric bio-molecular arrays are attracting intense interest due to their great potential in numerous applications including protein and DNA chips for proteomic and genomic analysis, biological sensors for pathogen detection, and 2D or 3D crystalline arrays for determination of protein structure. Because SPN naturally lends itself to forming nanometric arrays of functional molecules, a number of researchers have recently explored it as a means for either directly patterning or templating subsequent deposition of biomolecules [16,39–43]. For example, Demers *et al.* fabricated arrays of DNA using DPN [15]. Similarly, Liu *et al.* used SNG to create DNA arrays by performing the grafting step in a solution containing thiolated single stranded DNA which filled in behind

AFM tip to form an array with the DNA at the free end [40]. Liu *et al.* also used biotinated thiols as an ink to template the subsequent deposition of streptavidin on 50 nm spots and both DPN and NG have been used to create protein arrays by first generating patterns of hydrophillic regions (e.g., MHA) in a hydrophobic background (e.g., PEG) [41]. The patterned substrates were subsequently exposed to a solution containing proteins such as lysozyme or BSA, which only adsorbed to the hydrophobic regions. Using a similar approach, Wilson *et al.* created arrays of collagen proteins [42].

All of these systems represent a miniaturization of more conventional biomolecular arrays produced through other techniques of patterning such as micro-stamping. Although there are many important applications of sub-100 nm scale patterns, such as ultra-dense protein chips, they generally do not involve systems in which the feature sizes are commensurate with the dimensions of the biomolecules. Systems in which this is the case offer the possibility of controlled molecule-by-molecule assembly of macromolecular architectures, one that becomes all the more attractive if the both the position *and* orientation of the biomolecules can be controlled.

Viruses, which are supramolecular assemblies of macromolecules, are typically on the order of tens of nanometers in size and have a wide range of functional groups present on their surfaces that can be targeted as sites for attachment. In fact, by genetically modifying viruses, it is possible to express unique chemical groups at a small number of surface sites [44]. In the case of icosahedral viruses, these sites can be chosen to be symmetrically equivalent. Moreover, because viruses are produced biologically according to a genetic code, they are atomically precise and monodisperse. Hence viruses provide ideal nanometric building blocks for the investigating molecularly directed assembly of bio-molecular arrays using SPN templates. Cheung *et al.* demonstrated a generic, multi-step approach to assembling arrays of viruses on SPN templates [45]. First they introduced unique chemical groups on the virus surface. Then they designed a long-chain linker that would form a covalently bound SAM at a gold surface while present a functional head group that would react chemoselectively with the engineered chemical groups on the virus surface. Afterwards, they grafted that linker into a background SAM that resisted virus binding.

Cheung *et al.* used a system that consisted of gold coated mica for the substrate, functionalized alkyl thiols as the linkers, and genetically modified cow pea mosaic virus (Cys-CPMV) [44] as the adsorbate as shown schematically in Figure 8.13. Smith *et al.* had also used a similar scheme to template virus deposition [46]. The virus was genetically engineered to present cysteine residues (Cys) at geometrically equivalent positions on the viral capsomer as shown in Figure 8.14. Because the reaction between the sulfhydryl groups on the virus and maleimides is highly chemoselective [47], a sulfhydryl–maleimide chemoselective reaction scheme was utilized. Functional thiols produced through a novel solid-phase synthesis process (Figure 8.17) and applied by two-step nanografting linked the mutated virus onto the substrate while triethylene glycol (TEG) terminated thiols (Figure 8.15) were applied as the resist to the surrounding regions for prevention of non-specific adsorption [48]. Figure 8.4 shows a pattern of ca. 30-nm-width lines filled with the amine terminated thiol that extend 0.5–2.0 nm above the background TEG terminated layer.

Using the highly selective thiol–maleimide reaction, Cys-CPMV virus was chemoselectively attached on chemical templates containing the maleimido functionality. To demonstrate a proof of principle for the virus assembly scheme, Cheung *et al.* first fabricated a micron-scale chemical template by micro-contact printing 10 μm squares of the

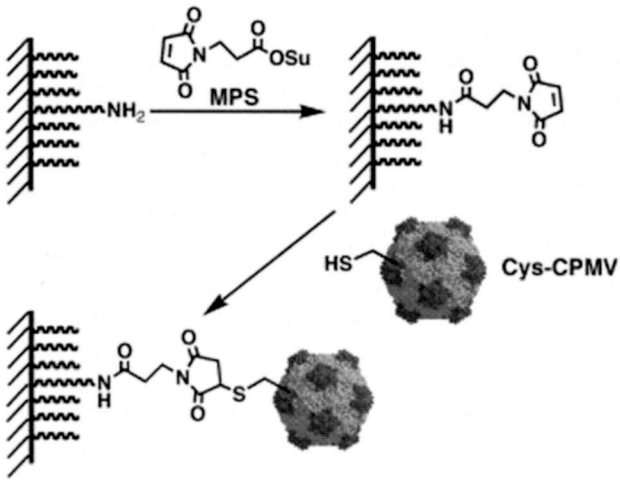

FIGURE 8.13. Scheme for attaching genetically modified virus (Cys-CPMV) to SPN templates on gold.

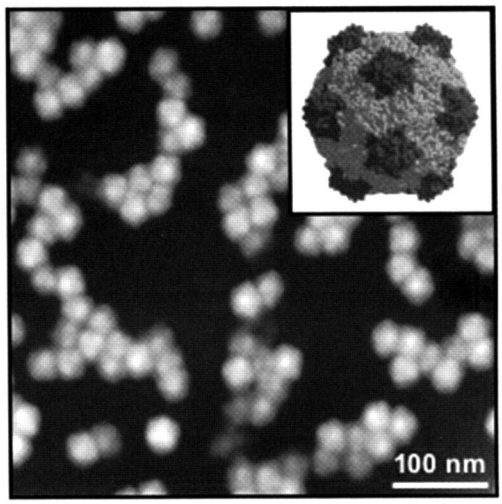

FIGURE 8.14. AFM height image of cow pea mosaic virus (CPMV). (Inset) Model of genetically modified CPMV virus with unique cysteine residues (Cys-CPMV). Red dots indicate the locations of mutated cysteine residues.

amino linker thiol on gold substrates and subsequently filling in the background with the TEG thiol. The maleimido function was then introduced by acylating the patterned amino groups with 3-maleimidopropionate N-hydroxysuccinimide ester (MPS). The chemical template was then treated with freshly reduced Cys-mutated CPMV in phosphate buffer at pH = 7.0 for 2 h, and the unbound virus was then washed away. As shown in Figure 8.16, the Cys-CPMV preferentially attached to the squares containing the maleimido function. Few virions were found in the background area. However, neither spatial correla-

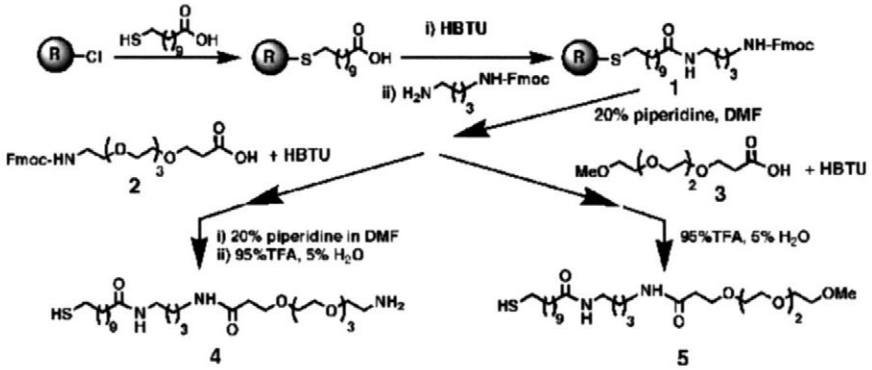

FIGURE 8.15. Scheme for synthesizing amino terminated and polyethylene glycol terminated inks. The former serves the virus linker and the latter functions as resist to virus binding.

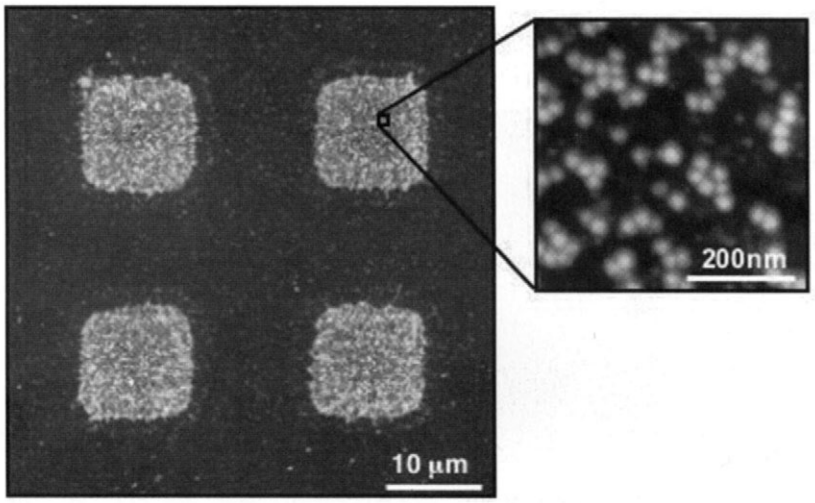

FIGURE 8.16. AFM height image of Cys-CPMV virus assembled on micrometer-sized template. (Inset) Magnified section of functionalized square.

tion, short-range order, nor long-range order between the viruses was observed within the squares.

When the dimension of the chemical template were reduced from the micron-scale to a size comparable to that of a CPMV, the morphology of virus assembly changed dramatically. Figure 8.17 shows an assembly of a dense population of the Cys-CPMV virions on most of the 30-nm-wide patterned lines made by nanografting and processed as the micron-sized templates. Probably due to size exclusion, a significant inter-virion attractive interaction, and the lack of an attractive virion-TEG interaction, the virions started to pack together into a close-packed morphology (Inset to Figure 8.17b). Not only did the lines themselves act as templates for attachment of the virions, but the lines of assembled virions then acted as templates for lateral growth of the viral assembly. As other virions

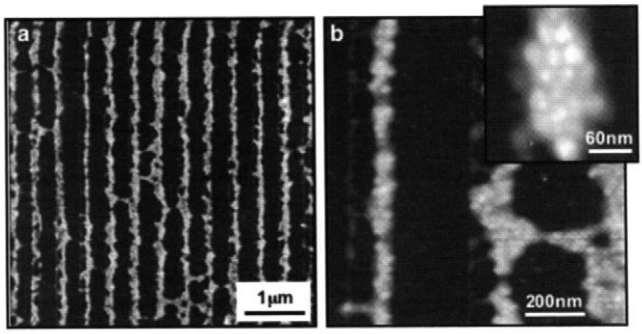

FIGURE 8.17. (a) AFM height image of a monolayer-thick virions assembled on a parallel line pattern created by nanografting with the chemoselective linkers. (b) Magnified section of Figure 8.17a. (Inset) Magnified image of another section of the same sample as in (b).

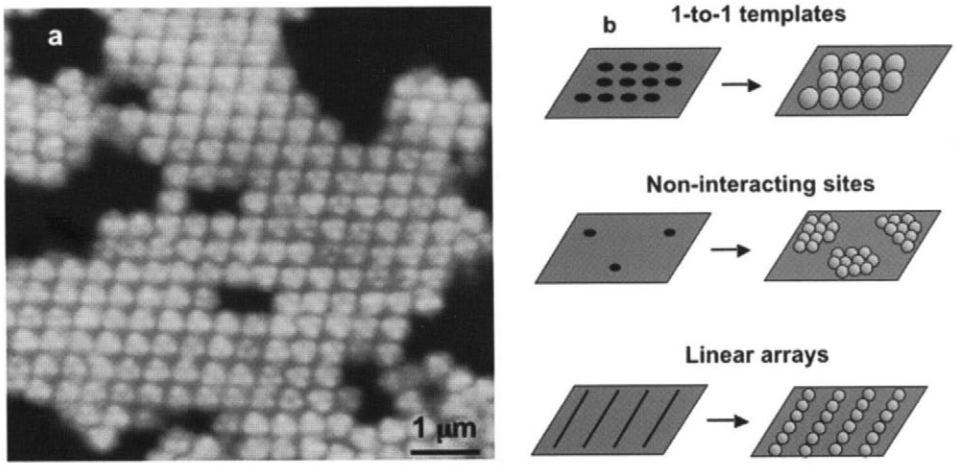

FIGURE 8.18. (a) Ordered islands of CPMV virus deposited on mica indicating tendency of virions to order under appropriate solution conditions. (b) Three potential methods to induce ordering at SPN patterns of linkers.

"stuck" to these lines, the lines "grew" laterally at the resulting step-edge and, in some cases, contacted adjacent lines of virions to form a pseudo-2D assembly (Figure 8.17b). Nevertheless, presumably because the attractive inter-virion interaction was too large, the lateral expansion did not proceed in a smooth and well-ordered manner.

Taking a lesson from the science of bulk crystallization of macromolecules, modulation of this strong inter-virion interaction by altering solution conditions such as pH and ionic strength could assist the creation of 1D nucleation templates for growth of ordered 2D crystalline films. Moreover, by varying these factors, as well as the concentration of virus in the solution during deposition, these templates can serve as platforms for investigating the physics of bio-molecular aggregation. As illustrated in Figure 8.19, by comparing the morphology and kinetics of assembly seen with *in situ* AFM with simulations of assembly using kinetic Monte Carlo methods, the strength of the virus–template and inter-virion

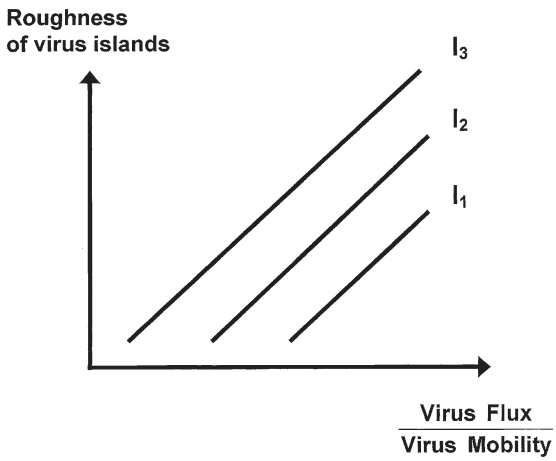

FIGURE 8.19. Schematic showing expected dependence of island roughness on virus flux and mobility. The flux is determined by the concentration and the mobility by the solution composition. I_x's, where $x = 1, 2$ and 3, represent the amount of precipitant in the virus solution with $I_3 > I_2 > I_1$. Analysis of nucleation and growth kinetics, as well as island morphology provides a means of probing the inter-virion and virus–template interactions through kinetic Monte Carlo modeling.

interactions can be estimated, and the importance of diffusion and attachment/detachment events evaluated.

8.7. CONCLUSION

In summary, scanning probe nanolithography has emerged as a versatile method for both direct patterning of soft structures and indirect templating of hierarchical structures at the nanoscale. It has been used to pattern a wide variety of compounds and biomolecules including alky thiols, organic dyes, proteins, antibodies, DNA, and viruses. In addition to providing a means of creating features at 10 to 100 nm length scales, this approach allows for generation of patterns with multiple functionalities opening up the possibility of producing ultra-dense DNA and protein chips, as well as platforms for combinatorial chemistry and protein crystallization using minute quantities of material.

While the physical mechanisms by which ink transfer proceeds during DPN remains an area for future research, for soluble compounds, the aqueous meniscus formed between the tip and substrate clearly plays an important role. Indeed, DNA patterning cannot be done without it. More work is needed to sort out the relative importance of thermal desorption and surface diffusion versus dissolution and bulk diffusion. Experiments that investigate meniscus formation directly through environmental electron microscopy will be critical to this effort.

SPN templates for biomolecular adsorption present excellent platforms both for technological applications as well as fundamental studies of macromolecular aggregation. The role of interactions between the adsorbate and the solvent, the template, and other adsorbates, as well as the impact of flux and adsorbate mobility can all be explored. Perhaps the most far-reaching outcome of this work, would be an ability to define a generic route

to ordering macromolecules at surfaces. Such ordered patterns could take the place of 3D crystals in the field of protein structure determination, especially when the 4th generation light sources become available later this decade.

ACKNOWLEDGEMENTS

The authors would like to thank Ivan Hromada for the SEM images of the cantilever. This work is performed under the auspices of the U.S. Department of Energy by the Lawrence Livermore National Laboratory under contract number W-7405-Eng-48.

REFERENCES

1. D.S. Ginger, H. Zhang and C.A. Mirkin, *Angew. Chem.* **43**, 30 (2004).
2. G.Y. Liu, S. Xu and Y.L. Qian, *Accounts of Chem. Res.* **33**, 457 (2000).
3. G. Binnig, H. Rohrer, C. Gerber and E. Weibel, *Appl. Phys. Lett.* **49**, 178 (1982).
4. G. Binnig, C.F. Quate and C. Gerber, *Phys. Rev. Lett.* **56**, 930 (1986).
5. T.R. Albrecht, S. Akamine, T.E. Carver and C.F. Quate, *J. Vac. Sci. Technol. A* **8**, 3386 (1990).
6. G. Meyer and N.M. Amer, *Appl. Phys. Lett.* **53**, 1045 (1988).
7. G. Meyer and N.M. Amer, *Appl. Phys. Lett.* **57**, 2089 (1990).
8. E.E. Ehrichs, S. Yoon and A.L. de Lozanne, *Appl. Phys. Lett.* **53**, 2287 (1988).
9. F.R.F. Fan and A.J. Bard, *J. Electrochem. Soc.* **136**, 3216 (1989).
10. R.C. Jaklevic and L. Ellie, *Phys. Rev. Lett.* **60**, 120 (1988).
11. B.L. Weeks, T. Rayment and M.E. Welland, *Nanotechnology* **13**, 38 (2002).
12. J.P. Rabe and S. Buchholz, *Appl. Phys. Lett.* **58**, 702 (1991).
13. D.M. Eigler and E.K. Schweizer, *Nature* **344**, 524 (1990).
14. R.D. Piner and C.A. Mirkin, *Langmuir* **13**, 6864 (1997).
15. L.M. Demers, D.S. Ginger, S.J. Park, Z.X. Li, S.W. Chung and C.A. Mirkin, *Science* **296**, 1836 (2002).
16. A. Noy, A.E. Miller, J.E. Klare, B.L. Weeks, B.W. Woods and J.J. De Yoreo, *Nano Lett.* **2**, 109 (2002).
17. H. Zhang, S.W. Chung and C.A. Mirkin, *Nano Lett.* **3**, 43 (2003).
18. A. Ivanisevic, K.V. McCumber and C.A. Mirkin, *J. Am. Chem. Soc.* **124**, 11997 (2002).
19. J.F. Liu, S. Cruchon-Dupeyrat, J.C. Garno, J. Frommer and G.Y. Liu, *Nano Lett.* **2**, 937 (2002).
20. P.V. Schwartz, *Langmuir* **17**, 5971 (2001).
21. P.A. Thiel and T.E. Madey, *Surf. Sci. Rep.* **7**, 211 (1987).
22. D. Beaglehole and H.K. Christenson, *J. Phys. Chem.* **96**, 3395 (1992).
23. J.R. Zimmerman and J.A. Lasater, *J. Phys. Chem.* **62**, 1157 (1958).
24. R.M. Pashley, *J. Colloid Interface Sci.* **78**, 246 (1980).
25. L. Xu, A. Lio, D.F. Ogletree and M. Salmeron, *J. Phys. Chem.* **102**, 540 (1998).
26. D.A. Grigg, P.E. Russell and J.E. Griffith, *J. Vac. Sci. Technol. A* **10**, 680 (1992).
27. R.D. Piner, J. Zhu, F. Xu, S. Hong and C.A. Mirkin, *Science* **283**, 661 (1999).
28. C.A. Mirkin, S. Hong and L. Demers, *Chemphyschem* **2**, 37 (2001).
29. J. Jang, S. Hong, G.C. Schatz and M.A. Ratner, *J. Chem. Phys.* **115**, 2721 (2001).
30. S. Rozhok, R. Piner and C.A. Mirkin, *J. Phys. Chem. B.* **107**, 751 (2003).
31. B.L. Weeks, A. Noy, A.E. Miller and J.J. De Yoreo, *Phys. Rev. Lett.* **88**, 255505 (2002).
32. R.D. Piner and C.A. Mirkin, *Langmuir* **13**, 6864 (1997).
33. L. Xu, A. Lio, D.F. Ogletree and M. Salmeron, *J. Phys. Chem.* **102**, 540 (1998).
34. J. Freund, J. Halbritter and J.K.H. Horber, *Microscopy Research and Technique* **44**, 327 (1999).
35. C. Tsonopoulos, *Fluid Phase Equilibria* **156**, 21 (1999).
36. C. Tsonopoulos, *Fluid Phase Equilibria* **186**, 185 (2001).
37. P.E. Sheehan and L.J. Whitman, *Phys. Rev. Lett.* **88**, 156104 (2002).
38. P.V. Schwartz, *Langmuir* **18**, 4041 (2002).
39. G.Y. Liu and N.A. Amro, *Proc. Natl. Acad. Sci. USA* **99**, 5165 (2002).

40. M.Z. Liu, N.A. Amro, C.S. Chow and G.Y. Liu, *Nano Lett.* **2**, 863 (2002).
41. K. Wadu-Mesthrige, N.A. Amro, J.C. Garno, S. Xu and G.Y. Liu, *Biophys. J.* **80**, 1891 (2001).
42. D.L. Wilson, R. Martin, S. Hong, Cronin-Golomb, C.A. Mirkin and D.L. Kaplan, *Proc. Natl. Acad. Sci. USA* **98**, 13660 (2001).
43. K.B. Lee, S.J. Park, C.A. Mirkin, J.C. Smith and M. Mrksich, *Science* **295**, 1702 (2002).
44. Q. Wang, T. Lin, L. Tang, J.E. Johnson and M.G. Finn, *Angew. Chem. Int. Ed.* **41**, 459 (2002).
45. C.L. Cheung, J.A. Camarero, B.W. Woods, T. Lin, J.E. Johnson and J.J. De Yoreo, *J. Am. Chem. Soc.* **125**, 6849 (2003).
46. J.C. Smith, K.B. Lee, Q. Wang, M.G. Finn, J.E. Johnson, M. Mrksich and C.A. Mirkin, *Nano Lett.* **3**, 883 (2003).
47. J.A. Camarero, in: *From Solid–Fluid Interfaces to Nanostructural Engineering*, Vol. II (Plenum/Kluwer Academic Publisher, New York, 2003) in press.
48. K. Prime and G.M. Whitesides, *J. Am. Chem. Soc.* **115**, 10714 (1993).